Planetary and Space Science 237 (2023) 105768

Contents lists available at ScienceDirect

Planetary and Space Science

journal homepage: www.elsevier.com/locate/pss

Polarization dependency of transverse scattering and collisional coupling to the ambient atmosphere from meteor trails — theory and observations

Gunter Stober [a,*], Robert Weryk [b], Diego Janches [c], Erin C.M. Dawkins [c,d], Florian Günzkofer [e], Jose Luis Hormaechea [f,g], Dimitry Pokhotelov [h]

[a] Institute of Applied Physics & Oeschger Center for Climate Change Research, Microwave Physics, University of Bern, Sidlerstrasse 5, Bern, 3012, Canton Bern, Switzerland
[b] Physics and Astronomy, The University of Western Ontario, 1151 Richmond Street, London, N6A 3K7, Ontario, Canada
[c] ITM Physics Laboratory, NASA Goddard Space Flight Center, Greenbelt, MD, USA
[d] Department of Physics, Catholic University of America, Washington, DC, USA
[e] Institute for Solar-Terrestrial Physics, German Aerospace Center (DLR), Neustrelitz, MV, Germany
[f] Estacion Astronomica Rio Grande, Rio Grande, Tierra del Fuego, Argentina
[g] Universidad Nacional de La Plata, La Plata, Argentina
[h] Institute of Physics, University of Greifswald, Greifswald, MV, Germany

ARTICLE INFO

Keywords:
Meteors
Transverse scatter meteor radar
Polarization
Ambipolar diffusion
Electron line density
Full-wave scattering model

ABSTRACT

Quantitative analyses of transverse scatter meteors to derive physically consistent solutions of the ambipolar diffusion coefficient, electron line density, and initial trail radius have been rare. In this manuscript, we present simulations using a full-wave scatter treatment of the transverse scatter meteor echo profiles for different background collision frequencies to account for the increase in ion-neutral and electron-neutral collisions over the typical specular meteor layer between 75–110 km. The altitude dependency of the ion-neutral collision frequency was adapted from recent multi-frequency radar observations by the European Incoherent Scatter Scientific Association (EISCAT). We generate look-up tables with parallel and transverse reflection coefficients for various collision frequencies in order to investigate how this quantity alters the meteor echo profile observed at different altitudes. We analyze 33 specular meteor observations collected with the Southern Argentina Agile Meteor Radar Orbital System (SAAMER-OS). Typical detections provide information about the meteor trajectory, enabling computation of both scattering angles, as well as the determination of precise meteoroid velocities. However, with the addition of two recently installed antennas which receive each polarization direction separately, we were able to also determine the ambipolar diffusion coefficient, electron line density, and initial trail radius, by performing a qualitative fit to the collected data. Finally, we demonstrate that utilizing the polarization information of a given echo produces a similar result to that of the triple-frequency observations made using the Canadian Meteor Orbit Radar (CMOR).

1. Introduction

Meteoroids entering the Earth's atmosphere are heated and decelerated by the impinging ambient atmospheric atoms and molecules, and those with sufficiently high kinetic energy are vaporized forming an ambipolar diffusing plasma trail. Most of the meteoroids are vaporized at the mesosphere/lower thermosphere (MLT) at altitudes between 70–120 km. Transverse scatter meteor radar observations of such trails have been carried out for decades to study the near Earth meteoroid environment and source characteristics of the meteor influx (McKinley, 1961; Jones and Jones, 1990; Webster et al., 2004; Campbell-Brown and Jones, 2006; Janches et al., 2015; Bruzzone et al., 2021) as well as using their line of sight Doppler velocity to determine atmospheric winds or decay time for temperatures (Hocking et al., 2001; Holdsworth et al., 2004) leveraging the reflection of transmitted electromagnetic waves from these cylindrical plasma columns. Although meteor radars have been deployed all around the world, there are still open questions related to the specular observation geometry and the scattering behavior, and how this scattering affects the derived parameters such as Doppler velocity, electron line density, ambipolar diffusion, initial trail radius, or the ambient collisions frequencies (Stober et al., 2021a, 2022).

By the late 1940s the first theories had been developed to understand the physics of electromagnetic wave scattering from cylindrical

* Corresponding author.
E-mail address: gunter.stober@unibe.ch (G. Stober).

https://doi.org/10.1016/j.pss.2023.105768
Received 1 June 2023; Received in revised form 21 August 2023; Accepted 4 September 2023
Available online 9 September 2023

plasma columns (Lovell and Clegg, 1948; Herlofson, 1951; Kaiser and Closs, 1952b). These results were summarized in McKinley (1961) and describe the signal at the receiver by radar-specific parameters such as frequency, antenna gain, transmitting power, and the classical electron scattering radius, as well as the meteor trail parameters of electron line density, initial trail radius, and the ambipolar diffusion coefficient. Furthermore, the trail reflects a characteristic oscillation, which can be described by the Fresnel integrals (McKinley, 1961), which also provides a possibility to measure precisely the velocity of the meteoroid (Hocking, 2000; Elford, 2004; Holdsworth et al., 2007; Stober et al., 2013; Mazur et al., 2020).

Later, Poulter and Baggaley (1977) proposed a full-wave scattering solution for transverse scatter assuming a Gaussian radial plasma distribution for meteor radar observations. They performed qualitative simulations and demonstrated that the scattering depends on the scattering angle between the incident electromagnetic wave (E-field vector and H-field vector) and the trail alignment and the gradient in the electron line density, thus indicating a strong polarization dependence of the derived reflection coefficients. The two polarizations were denoted parallel and perpendicular reflections, corresponding to their observation geometry. Furthermore, the full-wave scattering equations describing the plasma inside the meteor trail are derived from Maxwell's equations in cylindrical coordinates (Kaiser and Closs, 1952a; Poulter and Baggaley, 1977; Stober et al., 2021a). These equations show a singularity in the complex permittivity for transition echoes from overdense to underdense for the transverse scattering case, giving rise to significant resonance effects. Such resonances were discussed in Greenhow and Hall (1960) and are expected when the critical radius leads to a vanishing real part of the complex dielectric function. In the past, the difference between overdense and underdense was defined by a threshold electron line density of $q = 10^{14}e^-/m$, which is more an instrumental effect rather than a true physical threshold (Poulter and Baggaley, 1977; Baggaley, 2002).

The first quantitative reflection coefficients, covering typical meteor radar frequencies using the full-wave scattering model, were presented more than 40 years later by Stober et al. (2021a). The authors included a comparison of different radial plasma models, which analyzed for a three-dimensional finite difference time domain (FDTD) model (Marshall and Close, 2015; Marshall et al., 2017). Later analytical and numerical calculations for meteor head echo plasmas showed that the radial distribution appears to be dependent on the observation geometry as well (Dimant and Oppenheim, 2017a,b; Sugar et al., 2018). Sugar et al. (2019) performed numerical simulations of meteor head echoes investigating how the radial plasma distribution changes depending on the viewing geometry relative to the flight path, which also included the specular geometry. Later, these solutions for the radial plasma distribution were used in the full-wave scattering model and resulted in a very close resemblance to the analytical solution of the cylindrical diffusion equation, which is given by a Gaussian radial plasma distribution (Stober et al., 2021a). Thus, the analysis presented herein is based on simulations using the Gaussian model putting a strong emphasis on the importance of the collisions on the obtained reflection coefficients. We also will show a vertical profile of ion-neutral collision frequencies derived from multi-frequency EISCAT data (Grassmann, 1993; Nicolls et al., 2014).

The Southern Argentina Agile Meteor Radar (SAAMER) at Tierra del Fuego (TDF) is located at the southern tip of Argentina (53.7 °S, 67.7°W), and the system has been widely used for atmospheric observations to investigate gravity waves generated over the Andes and the Drake passage (Fritts et al., 2010; de Wit et al., 2016; de Wit et al., 2017; Liu et al., 2020, 2022; Stober et al., 2021c, 2022). The meteor radar has remote receiver sites at distances between 8 to 13 km around the core antenna array that enables the precise orbit determination of the detected meteors. This configuration is called SAAMER-OS (SAAMER-Orbital System) (Janches et al., 2014; Janches et al., 2015; Bruzzone et al., 2021; Panka et al., 2021). Another update to SAAMER was made during the 2022 southern hemispheric winter season: two antennas were installed next to the main receiver array, each one receiving data from each polarization separately. In this work, we use these observations together with the orbital data to estimate the scattering angle and to perform a qualitative fit to the observations to determine the electron line density (q), initial trail radius (r_0), and the ambipolar diffusion coefficient (D).

The manuscript is structured as follows. Section 2 contains information about the radar calibration applied in this study. The importance of collisions for calculating reflection coefficients is outlined in Section 3 and the full-wave scattering results are shown in Section 4. The resulting implications for the diffusion measurements using the classical theory are given in Section 5. The observational results are shown in Section 6. The results are discussed and summarized in the last two Sections 7 and 8.

2. Observation and calibration

In this study, we analyze data by making use of the full capabilities of SAAMER-OS. A detailed description of the initially deployed instrument is found in Fritts et al. (2010). Later the system was upgraded by adding passive remote receiver sites at distances between 8 to 13 km to determine the meteor trajectories (Janches et al., 2015; Bruzzone et al., 2021), which is called SAAMER-OS. The capabilities of the radar were continuously enhanced by adding more passive receiver stations a few kilometers away from the main site and software developments (Panka et al., 2021).

During the southern hemispheric winter in 2022, two new receiving antennas were installed next to the main receiver array that is set up using a modified Jones cross (Jacobs and Ralston, 1981; Jones et al., 1998). The new antennas measure each polarization plane independently to a separate receiver located in the main electronics hut (Janches et al. (2015), Fig. 3). Thus, in total we record 7 complex raw voltages for each detected meteor. The 5 antennas that are part of the initial Jones array are circularly polarized (Fig. 1). For the transmission, a single circularly polarized Yagi antenna is used, instead of the originally deployed transmitting array for momentum flux observations consisting of 8 Yagi antennas arranged in a circle (Fritts et al., 2010).

The SAAMER-OS receiver chain was calibrated using two methods, which were already applied in previous studies on different radars (Swarnalingam et al., 2009; Stober et al., 2011). The first calibration approach is based on a calibrated noise generator signal that is directly fed into the receivers. By tuning the noise generator through different but well-defined noise powers, it is possible to characterize the receivers. The second method leverages a natural noise source given by the cosmic radio noise background. De Oliveira-Costa et al. (2008) compiled a Global Sky noise Model (GSM) merging several calibrated radio noise observations, which provides a sky noise temperature in the frequency range between 10 MHz to 100 GHz and sufficient angular resolution. The GSM is accurate within 1%–10% over a wide range of frequencies and certain areas of the sky. During the course of the day, the receiver antenna beam points towards different parts of the sky and, hence, to regions in the sky with different sky noise temperatures. The QDC (Quiet Day Curve) that is required for the calibration is obtained by convolving the antenna pattern of the circularly polarized Yagi antennas over the computed noise map for different sidereal times.

The cosmic noise calibration was done similarly to the Collm radar (Stober et al., 2011). We calculated a QDC for the SAAMER-OS location convolving the circularly polarized beam with the GSM sky noise temperature map to obtain our calibration reference QDC_{GSM}. The SAAMER-OS QDC was derived using the meteor-position-data-files (MPD) to estimate the noise power for each meteor. This data was then binned in solar longitude and sidereal time, the UTC time was documented, and we computed a median value of the noise power

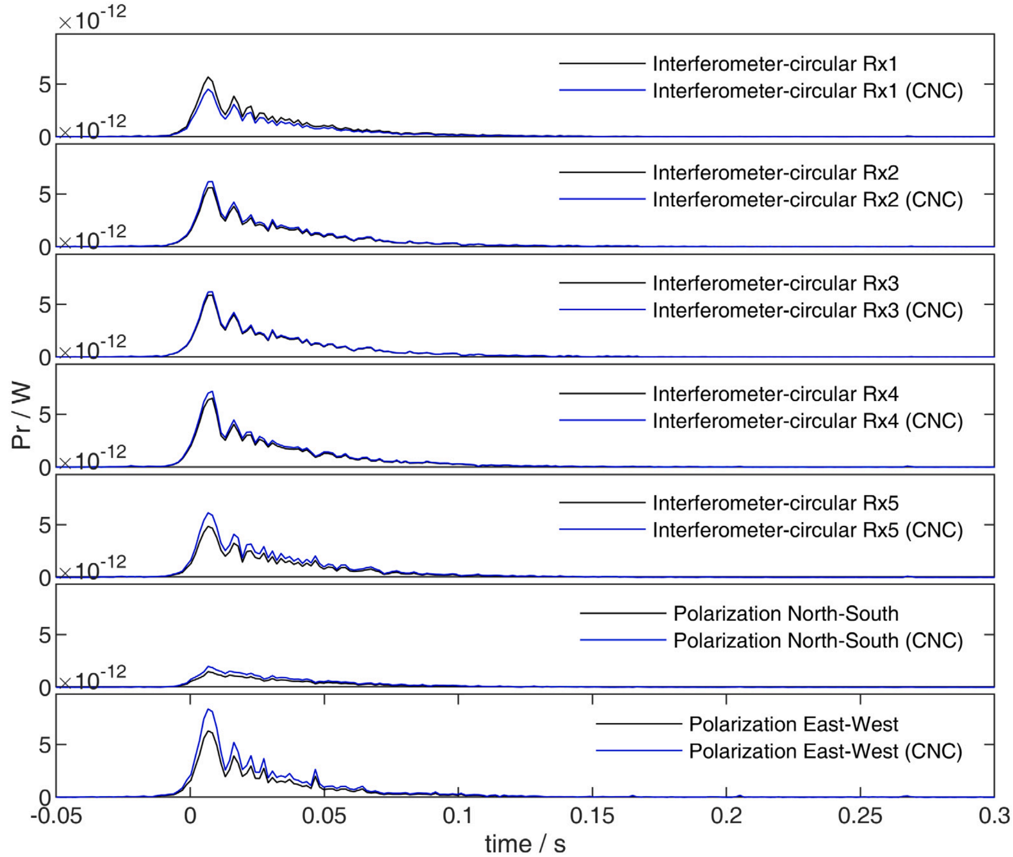

Fig. 1. Meteor signal received by the main receiver at the main site of SAAMER-OS. The first five raw voltages show the signal strength of the meteor received by each of the five antennas that form the interferometer. The last two rows show the signal strength on each polarization received by the two new antennas.

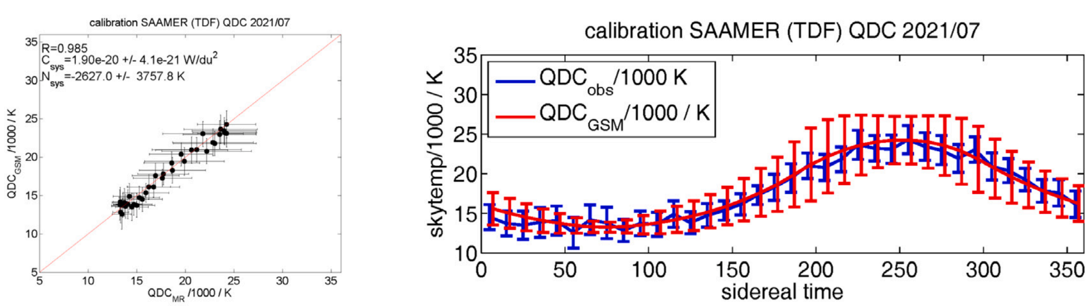

Fig. 2. Correlation and comparison of the GSM-derived QDC and the cosmic noise calibrated SAAMER-OS observations.

in digitizer units (du) for each bin and a corresponding standard deviation. The resulting noise time series has a resolution of 10° in sidereal time.

Fig. 2 shows a linear regression and comparison of the QDC derived from the GSM and SAAMER-OS. The calibration coefficient was estimated from the long noise record for periods with no radio interference. We compiled a monthly averaged QDC from the observations corresponding to about 30° in solar longitude but rejected all observations that showed an anomalously large standard deviation or a deviation of more than 75du from the median value for that bin. We did not remove the solar contribution for the calibration as the solid angle of the corona is considerably smaller than our beamwidth and thus is not critical for the calibration. The presented QDC corresponds to the southern hemispheric winter season of July–August 2021.

3. Collision dependence of polarization strength full-wave scattering

The full-wave scattering theory developed by Poulter and Baggaley (1977) describes the scattering of radio waves from infinitely long cylindrical plasma trails. This theoretical framework indicated that the scattering depends on the angle between the incident radio wave and the alignment of the meteor trajectory. As such, the reflection coefficients are separated into transverse/perpendicular and parallel components with respect to the meteoric plasma column. However, due to computational limitations at the time, only qualitative estimations were shown. Recently, the proposed full-wave scattering model was used to perform quantitative simulations of reflection coefficients for the triple frequency meteor radar CMOR (Canadian Meteor Orbit

Radar) (Stober et al., 2021a) to derive a physically consistent solution for the ambipolar diffusion coefficient, the electron line density, and the initial trail radius. These quantitative simulations were performed for various plasma distributions that were originally proposed to better describe the scattering from meteor head echoes such as Gaussian, parabolic exponential, 1/r, 1/r2, and the 1/r3 model (Marshall et al., 2017; Sugar et al., 2019).

Meteor trails are assumed to form instantaneously and start to diffuse in a radial direction along the meteoroid flight path. The released ions and electrons form an ambipolar plasma that diffuses quickly into the ambient atmosphere. The electrostatic force between the ions and electrons ensures that the electrons diffuse effectively with the ions, although the mobility of the electrons is much higher compared to the ions. As the electron density in the plasma column corresponds to the ions density ($n_e = n_I$), it is sufficient to solve the radial diffusion equation just for the electron density;

$$\frac{\partial n}{\partial t} = \frac{D}{r}\frac{\partial n}{\partial r}\left(r\frac{\partial n}{\partial r}\right), \tag{1}$$

Here r denotes the radial distance from the trail axis, D describes the ambipolar diffusion coefficient and n is the radial electron density. The analytical solution of the above equation assuming a Gaussian function for the electron density distribution normalized to the electron line density q is given by;

$$n(r,t) = \frac{q}{\pi a^2} \cdot e^{\frac{-r^2}{a^2}}. \tag{2}$$

The temporal dependency of the Gaussian plasma distribution is expressed by the simple relation;

$$a^2 = r_0^2 + 4Dt. \tag{3}$$

Here r_0 is the initial trail radius and a denotes a generalized trail radius. However, we can omit the time-dependent part and use only the radius for the full-wave scattering model. Computing the reflection coefficients for different radii a is equivalent to the time-dependent expansion of the trail without the need to explicitly solve the time-dependent radial plasma distribution.

The electron motion inside the column is governed by the complex dielectric constant (Poulter and Baggaley, 1977);

$$\kappa(r) = 1 - \frac{ne^2}{\epsilon_0\, m\omega^2(1 + i\nu/\omega)}. \tag{4}$$

Here e is the elementary charge and m is the electron mass, ϵ_0 is the free space permittivity, ω denotes the incident wave angular frequency, and ν are collision frequencies. The collision frequencies used in the full-wave scattering solution are derived as proposed in Marshall and Close (2015). The electron-neutral collisions are estimated to be in the order of $\nu_{en} \approx 6 \cdot 10^4\ \mathrm{s}^{-1}$ at 100 km altitude assuming an MSIS-E-90 background atmospheric temperature (Hedin, 1991). Above 100 km the electron-neutral collision frequency crucially depends on the O_2/N_2-ratio. Below 100 km the electron-neutral collision frequency is mainly a function of the neutral density and the electron temperature (Schunk and Nagy, 2009). Furthermore, Marshall and Close (2015) emphasized the importance of the Coulomb collisions between electron–electron and electron–ion collisions pairs, which are estimated following the relations presented in Callen (2006) and can be derived from the meteor plasma properties.

Ion-neutral collisions are also important for the evolution of the trail in the radial direction from the trail axis. Increased ion-neutral collisions result in a slower ambipolar diffusion and vice versa. Ion-neutral collision frequency profiles can be directly or indirectly measured using Incoherent Scatter Radars (ISRs) such as the ones operated by the EISCAT Scientific Association (Nygrén, 1996; Oyama et al., 2012; Nicolls et al., 2014). Fig. 3 shows a vertical profile of the ion-neutral collision frequency derived from dual-frequency ISR observations applying the data analysis proposed by Grassmann (1993). The data were

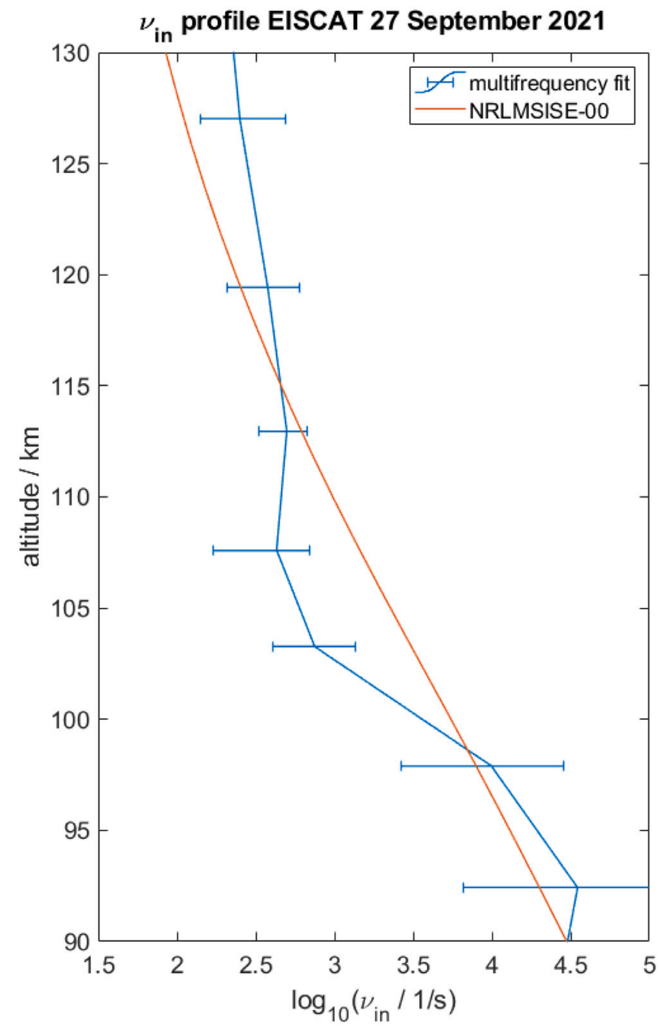

Fig. 3. Vertical profiles of ion-neutral collision frequencies. The measurement profile (blue) is derived from dual-frequency EISCAT observations on 27 September 2021 between 8–12 UTC with error bars indicating the interquartile range. A climatological collision frequency profile (orange) is calculated from the NRLMSISE-00 model neutral particle density.

recorded during a campaign on 27 September 2021 between 8–12 UTC involving the TromsøEISCAT VHF (Very High Frequency) (224 MHz) and UHF (Ultra High Frequency) (930 MHz) radars (at geographic coordinates 69.58°N, 19.22°E). The figure shows the median profile of all measurements during the four-hour observation window from 08–12 UTC. The analysis follows the difference spectrum method as described in Grassmann (1993). The ion-neutral collision frequencies based on NRLMSISE-00 are obtained from the idealized relation of Chapman (1956), which involves a mean atomic mass as well as neutral and ion volume number densities. We found that the ion-neutral collision frequency changed by two orders of magnitude across the meteor layer region (80–110 km). Similar behavior is also expected for the electron-neutral collision frequency. Expressing the electric and magnetic fields inside the column by Maxwell equations in cylindrical coordinates as parallel P_m and transverse T_m components corresponding to the plane of the oscillation of each of the field vectors of the incident electromagnetic wave leads to two second-order differential equations. The field inside the meteor trail for parallel geometry, which corresponds to an electric field oscillating in the plane of the meteor trajectory, is given by;

$$\frac{d^2\mathbf{P_m}}{dr^2} + \frac{1}{r}\frac{d\mathbf{P_m}}{dr} + \left(k^2\kappa - \frac{m^2}{r^2}\right)\mathbf{P_m} = 0. \tag{5}$$

The transverse case leads to the following differential equation;

$$\frac{d^2\mathbf{T_m}}{dr^2} + \left[\frac{1}{r} - \frac{1}{\kappa}\frac{d\kappa}{dr}\right]\frac{d\mathbf{T_m}}{dr} + \left(k^2\kappa - \frac{m^2}{r^2}\right)\mathbf{T_m} = 0. \tag{6}$$

Here k is the wavenumber of the incident electromagnetic wave, r is the radial distance from the trail axis, and m describes the order of Fourier components and the cylindrical Bessel and Hankel functions. Following Poulter and Baggaley (1977), Stober et al. (2021a) the fields outside the plasma column of the incident wave are described by cylindrical Bessel functions, and the reflected waves can be expressed by the Hankel functions of the first kind. Finally, we obtain reflection coefficients p_m and t_m after integrating Eq. (5) and 6 until the boundary matching radius for each order of the Hankel and Bessel functions. Adding all the complex reflections coefficients results in the total reflection coefficient $g_\parallel$ for the parallel and $g_\perp$ for the transverse geometry;

$$g_\parallel = \sum_m p_m \cos(m\phi) \tag{7}$$

$$g_\perp = \sum_m -t_m \cos(m\phi)$$

In this study, we only consider backscatter geometry $\phi = 180°$. Although, the derivation was performed assuming a plane incident wave the solutions can be generalized to arbitrary geometries and circular polarization (Poulter and Baggaley, 1977). Thus, the reflection coefficient g for an arbitrary alignment between the incident plane wave and the meteor trajectory is given by;

$$g = g_\parallel \cdot cos^2(\delta) + g_\perp \cdot \sin^2(\delta). \tag{8}$$

Here δ describes the angle between the electric field of an incident plane wave and the meteor trajectory.

4. Calculation of reflection coefficients for different collision frequencies

Reflection coefficients are obtained by solving the two differential equations for P_m and T_m for each order m of the cylindrical Bessel function as outlined in Stober et al. (2021a). The integration starts at the trail axis with $r = 10^{-10}$ m until the boundary matching radius r_b, which is defined as the distance from the trail axis where the dielectric function of the meteoric plasma equals the free space permittivity $\epsilon_r = 1$. We consider that this is achieved when the real part approaches $\kappa = 0.99999$. The numerical integration is performed with a 5th order Runge–Kutta scheme (Cash and Karp, 1990) calculating the first 19 orders of the cylindrical Bessel function starting by m=0.

In this study, all results refer to a meteor radar operating at 32.55 MHz, but use the collision frequencies that were given in Marshall and Close (2015), Marshall et al. (2017), Stober et al. (2021a) as a reference. These collision frequencies are representative of the altitude region between 100–110 km and match the peak height of meteor head echo observations (e.g. Janches et al., 2003, 2008; Schult et al., 2017; Kero et al., 2013, 2012). Specular or transverse scatter meteors are often observed at lower altitudes with an observational peak around 90 km (e.g. Hocking et al., 1997; Stober et al., 2012; Dawkins et al., 2023) and, thus, we adopted the collision rates to account for the increased atmospheric density at these lower altitudes by increasing them.

Fig. 4 compares parallel g_E and transverse g_H reflections and their polarization for the standard reference case and a Gaussian plasma distribution. The polarization p is obtained from the ratio of the transverse and parallel reflection coefficient ($p = g_\perp/g_\parallel$). The lower panels show the same but for a tenfold increased total collision frequency which corresponds approximately to 85–90 km altitude. The polarization ratios shown in the right column only contain data for reflection coefficients that are larger than 10^{-4}. A polarization value of 1 corresponds to circular polarization or to the case that the scattering is more isotropic. However, due to the specular geometry, isotropic scattering is rarely achievable independent of the collision frequencies. However, increased collision frequencies reduce the resonance effect that occurs at the critical radius r_c in the transverse scatter case (g_H) when the real part of κ is essentially zero. These resonance effects are typical for the transition from overdense to underdense scattering (Kaiser and Closs, 1952a; Poulter and Baggaley, 1977; Stober et al., 2021a). The simulations also confirm that increased collision frequencies lead to an even stronger polarization ratio for small trail radii and electron line densities above $10^{12} e^-/m$.

We also compare individual profiles for different electron line densities $q = 9 \cdot 10^{12}$, $q = 9 \cdot 10^{13}$ and $q = 9 \cdot 10^{14}$ e^-/m. These line densities correspond to a typical underdense, a transition, and an overdense specular meteor echo. However, we want to emphasize that the terms underdense and overdense always refer to a certain initial radius and an electron line density. In principle, even a lower electron line density leads to overdense scattering characteristics when the meteor plasma remains confined in close proximity to the meteor trail axis (a few millimeters to a few centimeters corresponding to the 1-σ width of the Gaussian plasma distribution). This is more likely to happen at altitudes below 85 km where the mean free paths reaches such scales. Fig. 5 visualizes all three cases as a function of radial distance from the trail rather than its temporal evolution due to ambipolar diffusion. Each of the panels contains the profiles for our reference collision model and for the 10× increased case for the parallel and transverse reflection coefficients. These profiles again support that the transverse scattering geometry is more efficient compared to the parallel case. In general, it is obvious that increased collisions result in smaller peak amplitudes and, hence, smaller reflection coefficients. In contrast, the resonance effects for the overdense meteor electron line densities are much less pronounced for the transverse geometry. These profiles also underline that the polarization is most significant during an earlier stage of the trail formation corresponding to smaller radii and becomes less important as the trail radially expands from the trail axis.

5. Implications of scattering results for ambipolar diffusion measurements

Meteor radars are also valuable to obtain a mean MLT temperature (Hocking et al., 2004; Stober et al., 2008, 2017; Sarkar et al., 2021). There are two established methods, which are based on the measured decay time of underdense meteors and an empirical temperature gradient model (Hocking et al., 1997; Hocking, 1999) or by using an empirical pressure model together with the ambipolar diffusion coefficient obtained from the decay time (Holdsworth et al., 2006) to derive a mean temperature from the data. However, both methods rely on the assumption that the meteor decay time is directly proportional to the ambipolar diffusion coefficient D_a. The classical meteor theory is based on a rather simple relation for the echo profile of an underdense meteor (Herlofson, 1951; Kaiser, 1953), which is still used today;

$$P(t) = P(0)e^{-\frac{32\pi^2 D_a}{\lambda^2}t}. \tag{9}$$

Here P denotes the backscatter power, t is the time, and λ is the radar wavelength. Thus, the ambipolar diffusion coefficient can be obtained by measuring the decay time of the fading meteor signal as long as the meteor is “underdense”. Considering the results from the full-wave scattering such a classification is not as straightforward as it appears and is not just given by a simple threshold of the electron line density as it was done previously;

$$\tau_{1/2} = \frac{\lambda^2 \ln 2}{32\pi^2 D_a}. \tag{10}$$

Furthermore, due to the high collision frequencies between the ions and neutral atmosphere in the MLT and for a vanishing electric field, we can use the Einstein relation for the ionic diffusion (Chilson et al., 1996);

$$D_i = \frac{k_B T}{e}\left(\frac{T}{273.16\ \mathrm{K}}\right)\left(\frac{1.013 \cdot 10^5\ \mathrm{Pa}}{p}\right) \cdot K_0 \tag{11}$$

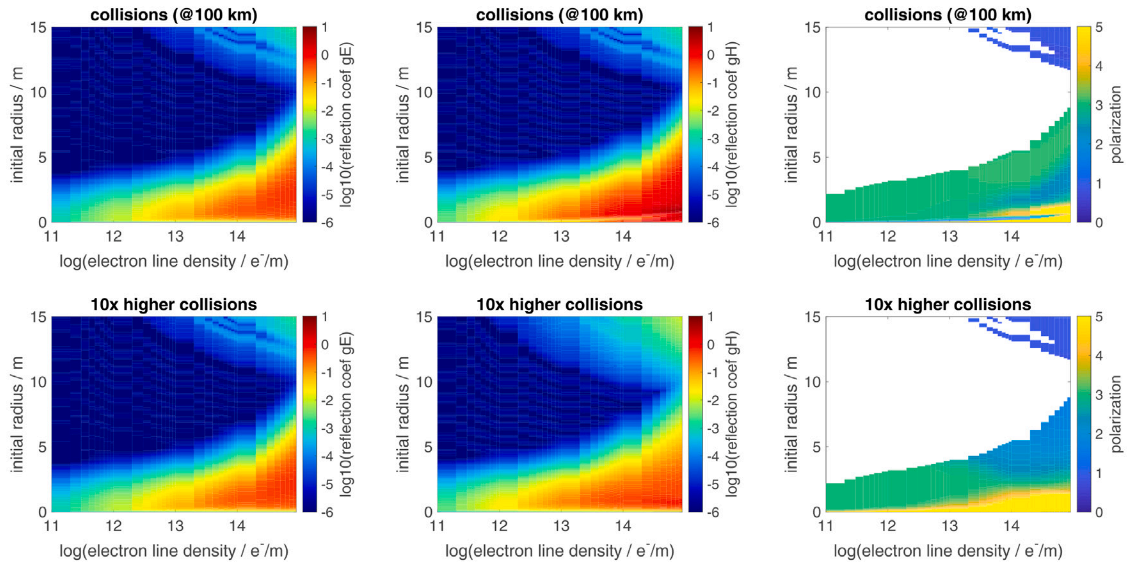

Fig. 4. Parallel (left) and transverse (center) reflection coefficients for typical specular meteor observations and corresponding polarization (right). The lower row shows the same but for a 10× increased collision frequency corresponding to lower altitudes.

Where D_i is the ionic diffusion coefficient, K_0 is the zero-field reduced ion mobility, k_B is the Boltzmann constant, e is the elementary charge, p is the total atmospheric pressure and T denotes the local thermal equilibrium temperature of the neutral gas. The above equations remain valid only for highly collisional meteor plasmas, for which it is reasonable to assume $D_a = 2 \cdot D_i$ (Kaiser, 1953). Neglecting electron–ion collisions, we can then approximate the ambipolar diffusion coefficients using the following expression (Jones, 1975, and references therein);

$$D_a \approx D_i\left(1 + \frac{T_e}{T_i}\right). \tag{12}$$

Here T_e and T_i are the electron and ion temperatures, respectively. Jones (1975) noted that the assumption of $T_e = T_i$ is not always satisfied within the MLT, and attributed some of these deviations at lower altitudes below 90 km to oxidation and dissociative recombination effects. The terms lower and higher altitudes refer to the typical meteor layer extending from 70 to 110 km. However, it is not possible to specify absolute altitude thresholds due to the high atmospheric variability, which also affects neutral density and, thus, the collision frequencies. Observations of the neutral density or neutral density proxies indicated a variability of about 20% corresponding to 1–3 kilometers in altitude (Stober et al., 2012; Vida et al., 2021; Dawkins et al., 2023). At lower altitudes of the meteor layer below 90 km, the ambipolar diffusion is slow enough for some echoes that such effects start to become relevant. At higher altitudes, the appearance of secondary reflection points caused by wind shears becomes important as well. However, many previous studies did not account for a potential effect or difference between transverse and parallel reflection coefficients and the resultant diffusion coefficients (Chilson et al., 1996; Hocking et al., 1997; Laskar et al., 2019; Lee et al., 2016). Furthermore, previous studies reported that ion–electron collisions (Coulomb collisions) and electron–electron collisions are important during the initial trail formation for the meteoric plasma (Marshall and Close, 2015) and, thus, are included in the full-wave scattering simulation (Stober et al., 2021a).

Considering the results from the full-wave scattering model for the transverse and parallel scattering coefficients, we estimated a potential deviation of the T_e/T_i-ratio using the parallel case as a reference to estimate the asymmetry in the scattering between both geometries. We computed the $\tau_{1/2}$-decay time for both reflection coefficients from the auto-correlation function (ACF). Fig. 6 shows the corresponding T_e/T_i-ratios that are required to obtain the same ambipolar diffusion coefficient for the transverse scattering geometry when we apply Eq. (10). The white line indicates a deviation of 1%. Apparently, the ambipolar diffusion coefficient would be systematically overestimated for the transverse scatter case and typical underdense meteor echoes. The 'apparently' increased ambipolar diffusion is mainly caused by a 'hotter' electron gas compared to the ion temperatures as the electrons start to coherently respond to the incident radio wave. Although, the electrons show a strong resonance effect in the transverse scatter case, the space charge field still ensures that the ions and electrons diffuse with the same velocity (Jones, 1975).

Finally, we tested the general applicability of the classical theory to determine the ambipolar diffusion coefficient from the decay time of a meteor echo for various collision frequencies. Assuming the full-wave scatter solution as a reference, we can compute by how much the T_e/T_i-ratio has to change to obtain the same ambipolar diffusion coefficient. Fig. 7 shows the T_e/T_i-ratio that is required to get the same ambipolar diffusion coefficient as it was used for the simulation of the meteor echo of the full-wave scattering model. The dark bluish part indicates that the theory from Kaiser and Closs (1952a) holds and the meteor echo is underdense. The white line separates the underdense from the transition-type and overdense meteor echo region. Essentially a meteor becomes overdense when the dielectric function is zero, which is equivalent to the plasma frequency for a specific radar wavelength. The term transition-type meteors refers here to the full-wave scattering model solution to meteor trails that would be classified as underdense from their signal morphology, but that show signs of resonance effects leading to deviations in the derived ambipolar diffusion coefficients when analyzed with the classical theory.

Comparing the parallel and transverse reflection coefficients indicate that resonance effects in the transverse scatter geometry lead to a lower threshold electron line density for the transition between underdense and overdense. This transition was usually assumed to be at a fixed electron line density ($q = 2.4 \cdot 10^{14}$ m^{-1}) (Kaiser and Closs, 1952a; Poulter and Baggaley, 1977). However, the most pronounced effect is caused by changes in the collision frequency. Increasing the collision frequency shifts the transition threshold to lower electron line densities. Furthermore, parallel and transverse scatter reflection coefficients show increasing deviation in the T_e/T_i-ratio for the overdense region, which is caused by resonance effects.

Recently, multi-static meteor radar observations combining monostatic specular radars and passive receivers arrays at distances between 50–250 kilometers have been realized (Stober et al., 2021b, 2022). Full wave scattering calculations are also of importance for such forward

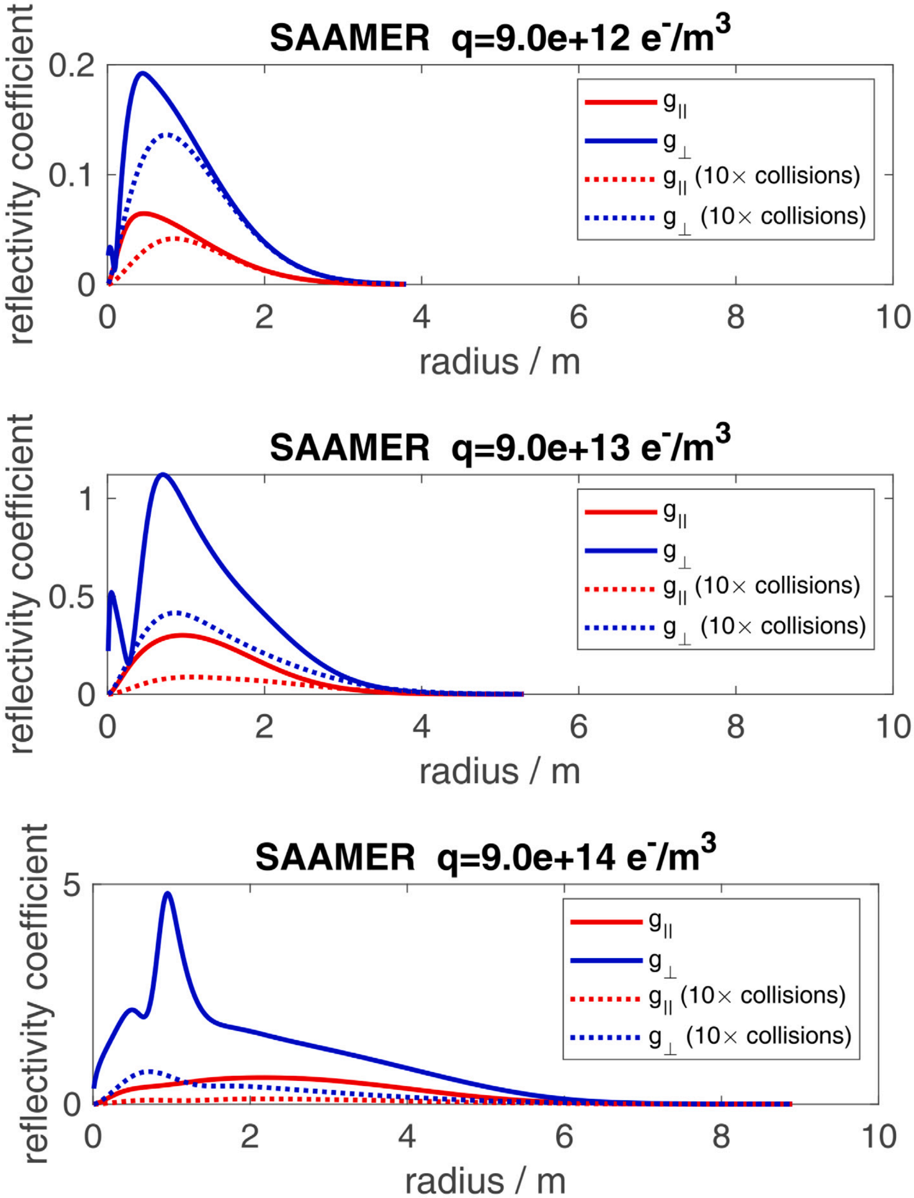

Fig. 5. Comparison of parallel and transverse reflection coefficients for different electron line densities of an underdense, a transition-type and overdense meteor echo and two different collision frequencies.

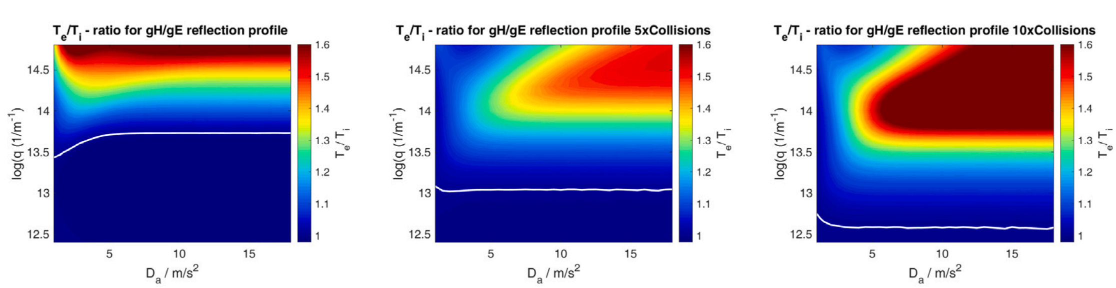

Fig. 6. Comparison of T_e/T_i-ratios derived from the decay time measurements of the ACF using the parallel case as a reference for typical values of ambipolar diffusion and electron line densities. The white contour line denotes a deviation of 1.05 T_e/T_i.

scatter observations (Jones and Jones, 1990), as the electron line density appears increased due to the forward scattering angle and, thus, multiple reflections can easily arise from different regions around the specular point as the meteor trail appears to be overdense, although a monostatic or backscatter system would classify it as underdense.

Specular meteor observations have become a widely used tool to measure mesospheric winds. Poulter and Baggaley (1978) investigated potential additional errors that can affect the wind measurements for different electron line densities and ambipolar diffusion coefficient and outlined mitigation strategies on how to correct the apparent line of

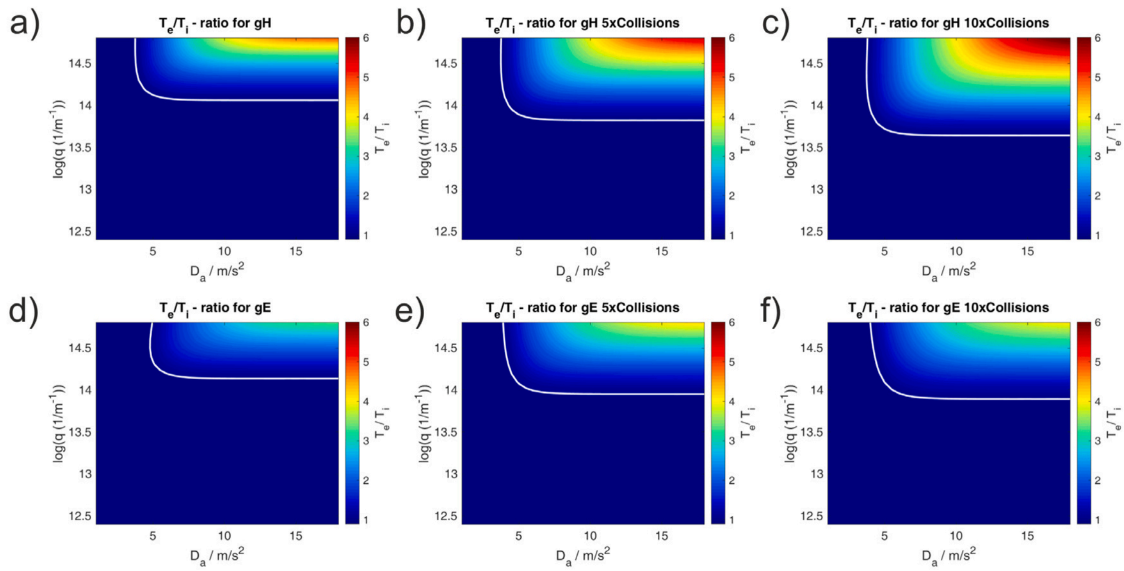

Fig. 7. Comparison of T_e/T_i-ratios derived from the decay time measurements of the ACF and the full-wave scattering ambipolar diffusion coefficient for different collision frequencies and transverse (a–c) and parallel (d–f) scatter reflection coefficients. The white contour line denotes a deviation of 1.05 T_e/T_i between the full wave scattering solution and the classical decay time approach (Kaiser's theory).

sight velocities for transition-type and overdense meteors. A similar effect was already reported in Stober et al. (2022) for forward scatter networks. These apparent line-of-sight velocities are basically the result of a motion of the scattering center along the trail due to diffusion, wind shear, or other distortions.

6. SAAMER-OS observations

SAAMER-OS provides time-of-flight solutions between the central transmitting station and several receiving-only remote sites from which meteor trajectory, velocity, and ultimately orbital properties are determined (Webster et al., 2004; Jones et al., 2005; Mazur et al., 2020; Bruzzone et al., 2021), which is key in calculating the angle between the transmitted incident radio wave and the meteor trajectory. The installation of two new dual polarization antennas next to the main receiving interferometer array, along with other upgrades to SAAMER-OS (Janches et al., 2020), now also permits the collection of both polarizations from the returned signal. In this work, we analyze the first batch of 33 meteor events for which we obtained a multi-station time of flight solution.

The data were fitted by extending the reflection coefficient look-up tables for 32.55 Mhz (Stober et al., 2021a). We added additional reflection coefficients with increased collision frequencies by multiplying them with 2, 3, 4, 5, 10, 15, and 20 using the values from Marshall and Close (2015) as reference and representative for 105 km altitude. The remaining analysis procedure is implemented according to Stober et al. (2021a). However, it turns out that the so-called t_0-time is more difficult to be determined due to noise and the onset of the diffusion (Mazur et al., 2020). We found that the best solution is usually within one pulse from our initial t_0-time pick. The reflection coefficients can be related to the backscattered power in Watts leveraging the well-known radar equation for transverse scatter observations (Ceplecha et al., 1998; Stober et al., 2021a);

$$P_R = \frac{g^2 \lambda^3 G_R G_T P_T}{32\pi^4 R_0^3} \cdot \left(\frac{C^2 + S^2}{2} \right). \quad (13)$$

Here g denotes the total reflection coefficient, λ is the radar wavelength, P_T is the transmitted power corrected for cable losses, which is nominally 64 kW for SAAMER-OS, and G_T and G_R are the antenna gains for transmission and receiving, respectively. R_0 defines the range of the specular point and C and S are the two Fresnel integrals. The main advantage of this equation compared to the more common versions presented in McKinley (1961) or Baggaley (2002) is that the reflection coefficient replaced the classical electron scattering cross-section and electron line density, which provides a much more physically consistent description of the time-dependency of the meteor echoes.

Fig. 8 shows four example fits of a total of 33 analyzed events. The upper panel always shows the mean backscattered power averaged from all five circularly receiving antennas of the Jones array. The lower two panels visualize the received power for each polarization separately. The label NS denotes the dipole aligned in a North–South direction, and EW indicates the East–West aligned dipole, respectively. The amplitude scaling is consistent for all three panels and is normalized to the circularly polarized signal, which shows the highest power. The black measurements reflect the received echo power using the noise generator calibration without antennas. The blue measurements are based on the cosmic noise background calibration considering the 7-bit Barker code. The red profile indicates the best manually obtained fit convolved with the SAAMER-OS antenna gain pattern and scaled by the transmitted power based on Eq. (13). The fit also includes the Fresnel oscillations leveraging the precise time of flight velocity (McKinley, 1961; Stober, 2009; Mazur et al., 2020). We also use the Fresnel oscillations to adjust the $t0$-pick by one or two pulses.

The initial trail radii, electron line densities, and ambipolar diffusion coefficients are in a similar range to the analyzed data from the triple frequency CMOR radar (Stober et al., 2021a). Most of the events are underdense. However, our subset tends to be biased towards faster meteors and altitudes above 90 km, due to our selection process. We searched for meteor events exhibiting Fresnel oscillations and the typical exponential decay. The Fresnel oscillations were also valuable to match or correct for potential offsets of the initial t_0-time picks. The presented examples demonstrate that polarization effects play a significant role and the amplitude of the same meteor can vary substantially between the different dipoles of a circularly polarized antenna.

In total, we collected 33 events covering all three echo types (underdense, transition, and overdense) and for altitudes between 76–104 km. In Fig. 9, we present vertical distributions of the derived ambipolar diffusion coefficients, initial trail radii, and electron line densities. We color-coded the different echo types blue (underdense), red (transition type), and cyan (overdense). The initial trail radii and ambipolar diffusion coefficients exhibit the characteristic altitude-dependency which

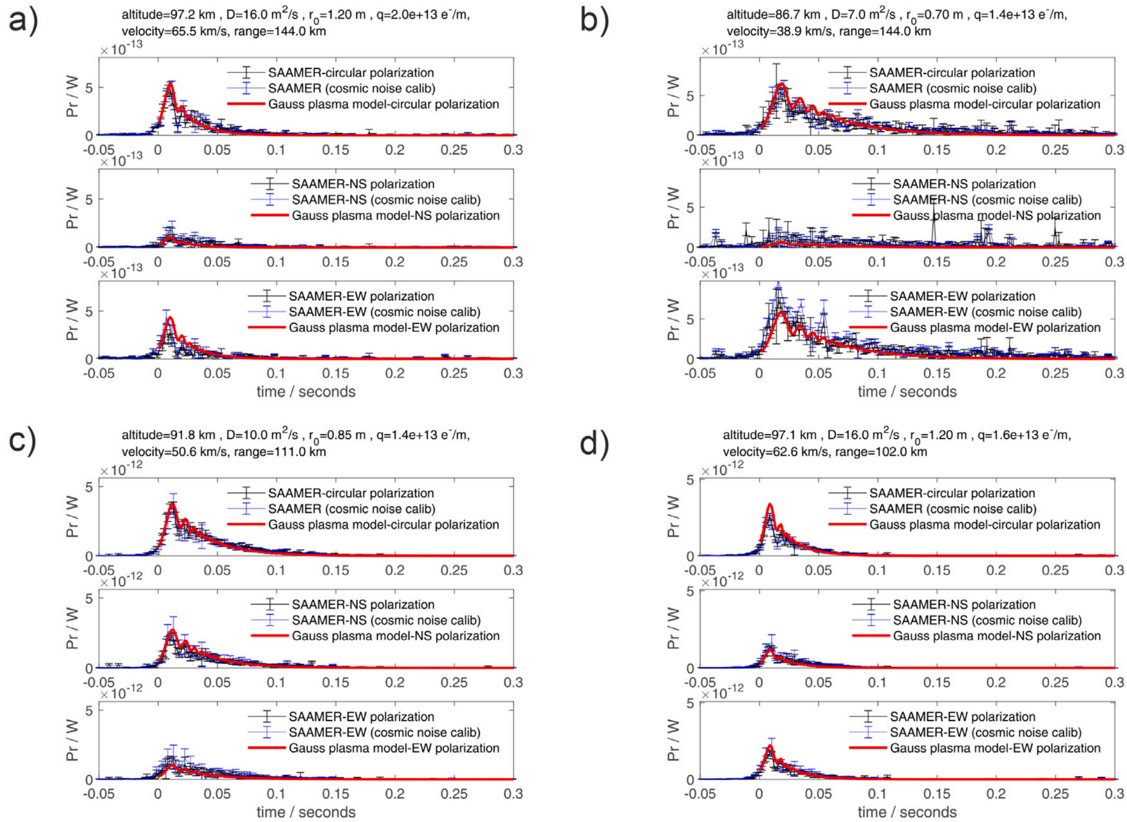

Fig. 8. Example fits of four different underdense meteors (a–d). Each of the examples has three panels showing the observations using the noise generator calibration (black), cosmic noise calibration (blue), and simulated full-wave scattering echo profile (red) for the circular receiver array (upper), the North–South (NS) dipole (center) and East–West (EW) dipole (lower). The cosmic noise data is only shown for every third point.

was already found in Stober et al. (2021a). This is also supported by the initial trail radii which indicates a linear trend of larger values with increasing altitude. However, we found much less scattering at the same altitudes compared to our initial fits using CMOR data (Stober et al., 2021a) where we only used a fixed collision frequency, which was more suitable for higher altitudes. The comparison also supports that the full-wave scattering solutions with variable collisions are also applicable to transition-type echoes, which might exhibit signs of resonance effects. The extreme outlier of the ambipolar diffusion coefficient for the overdense meteor is understandable due to the missing electron–ion recombination and ozone chemistry for such high-density plasma trails with a longer lifetime (Jones, 1975; Baggaley, 2002). Thus, the ambipolar diffusion coefficient is severely overestimated as the loss of electrons due to the recombination or by ozone is not yet taken into account (Ye and Han, 2017). In future work, these chemical reactions can be added to the fits by changing the electron line density over time to model the loss of electrons due to these reactions for overdense meteors. A more detailed analysis of all 33 events will be given in a companion paper.

7. Discussion

While the relative importance of the radiative transfer due to collisions for the scattering coefficients is included in the scattering theory (Poulter and Baggaley, 1977), there have been no studies on how different collision frequencies can alter the meteor echo profile. Using the multi-frequency EISCAT observations to estimate an ion-neutral vertical collision profile, we scaled the implemented collision models for the full-wave scattering model to also include the typical specular altitudes down to about 80 km. The model results indicate that increased collisions reduce the resonance peak that is theoretically predicted and obvious for overdense meteors (Stober et al., 2021a). However, it was also possible to show that an exponential decay might not be sufficient to classify meteor echoes in underdense, transition-type, and overdense echoes. The simulations demonstrate that the transition from underdense to overdense meteors depends on the collision frequency, and not on a fixed electron line density. Considering the classical underdense meteor theory we estimated the transition from underdense to overdense by a deviation of the T_e/T_i-ratio (Kaiser, 1953; Chilson et al., 1996) between the parallel and perpendicular reflection coefficient. We found that the electrons respond to a perpendicular incident radio by a more coherent motion and can get in resonance for transition-type and overdense echoes, whereas in the parallel case, some of the energy is absorbed by the collisions within the plasma and, thus, the resultant reflection coefficient is smaller.

The full-wave scattering model is applicable to Continuous Wave (CW)- and pulsed radar observations. The fit of the simulated reflection coefficients to SAAMER-OS observations supports that the peak power defines the sensitivity of the system rather than the average power. The often smaller transmit power of CW-radars can be partly compensated by pulse compression. Another important difference between both experimental techniques is given by the collision frequencies. Pulsed radar systems use pulse repetition frequencies that are much lower than the typical collision frequencies in the meteoric plasma and, hence, the released meteoric ions and electrons can relax to the ambient atmosphere between successive pulses. It remains unclear whether resonance effects can cause issues for CW-radars at some altitudes for the magnetized electronic component and certain geometries (Stober et al., 2021a) or in the presence of other instabilities that can cause multiple reflection points along the trail and, thus, might lead to spurious Doppler velocities or more uncertain interferometric solutions.

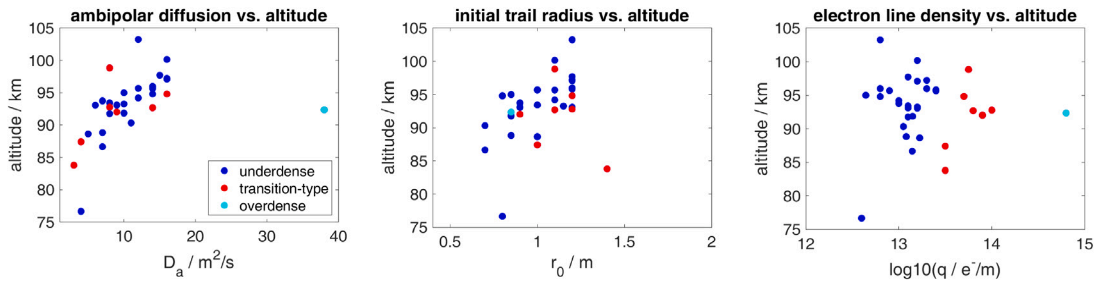

Fig. 9. Statistical analysis of all 33 events concerning the ambipolar diffusion, initial trail radii, and electron line density and their altitude-dependency with color codes for underdense (blue), transition-type (red), and overdense (cyan).

Ambipolar diffusion coefficients have been derived from meteor radar observations for decades, leveraging the theory from Kaiser (1953). This theory already included resonance effects and the separation of parallel and perpendicular scattering of the trail, and provided a simple relation between the exponential decay of the plasma and the ambipolar diffusion coefficients, which was applied in many observations of underdense meteor echoes to estimate vertical profiles (Chilson et al., 1996; Holdsworth and Reid, 2002; Lee et al., 2016; Laskar et al., 2019). However, the full-wave scattering model presented here underlines that it can be more difficult to separate underdense meteors from all detected meteors. Partly this explains the larger scattering of the ambipolar diffusion coefficient at the same altitude or decay times presented in many previous publications (Hocking et al., 1997; Hocking, 1999; Stober et al., 2008; Kumar and Subrahmanyam, 2012; Sarkar et al., 2021). The full-wave scattering model also indicates that it can be challenging to estimate the electron line density from the peak of the meteor echo profile (McKinley, 1961; Baggaley, 2002), which adds further complication in classifying underdense meteor echoes.

One of the open questions about specular observed meteor trails is the relative importance of the Earth's magnetic field on the ambipolar diffusion. Kaiser et al. (1969) showed that meteor trails that are closely field-aligned (to within 1° in the E-region) above 95 km altitude exhibit an anomalous ambipolar diffusion behavior as the electron motion is inhibited by the magnetic field. At this height, electrons become essentially magnetized while the ions are still demagnetized (Stober et al., 2021a). However, non-specular trails indicate a considerable dependence on the Earth's magnetic field as demonstrated by simulations and analytical theory (Dimant and Oppenheim, 2006b,a). The specular meteor trails analyzed in this study did include events that were close to being field-aligned and, thus, the magnetic field effect was not considered and is left for future studies.

8. Conclusions

Collisions between the meteoric plasma and the ambient atmosphere play a crucial role in understanding the echo profile of underdense meteors and how they diffuse. In this study, we investigated quantitatively how the polarization effects change with increasing collision frequencies compared to the typical values presented in previous studies (Marshall and Close, 2015; Stober et al., 2021a) and recent EISCAT observations. Full-wave scattering simulations have been conducted to generate complete sets of reflection coefficients for various collision frequencies that cover the altitude regions between 76–104 km.

The full-wave scattering simulations as well as SAAMER-OS observations underline that the signal amplitude is not necessarily a good quantifier of the electron line density to separate underdense from transition-type or overdense meteors without taking into account polarization effects. Furthermore, even transition-type echoes, which already show signs of resonance effects for the transverse scattering geometry, exhibit the classical textbook underdense signal morphology for higher collision frequencies (lower altitudes in the meteor layer), which causes larger deviations in the derived quantities of electron line density or ambipolar diffusion when analyzing these observations with the classical theory.

Resonance effects are an important aspect of specular meteor observations. In this study, we introduce a more clear separation of different meteor echoes based on their signal behavior. Overdense meteors are characterized by a plasma density inside the column that exceeds the plasma frequency for the radar wavelength. Underdense meteors have plasma densities much lower than the corresponding plasma frequency. Meteor echoes with plasma densities smaller than the plasma frequency for a defined radar wavelength that show already signs of resonance effects are considered transition-type meteors. Furthermore, the collision frequencies are crucial for the effective signal. Pulsed radar systems with pulse repetition frequencies much lower than the collision frequency will always observe a thermalized plasma in equilibrium with the ambient atmosphere. CW-radars might be useful for active target modification through these resonances, which could alter the diffusion and may cause instabilities along the trail leading to multiple reflections as seen for overdense meteor trails, in particular, at altitudes where the electrons are magnetized.

These simulations indicate substantial differences for parallel and transverse scattering geometry when the collision frequencies are varied, which also results in changes to the theoretically modeled echo profiles. Thus, altitude-dependent collision frequencies have to be taken into account when quantitative reflection coefficients are computed. Currently, there are only limited observational capabilities to determine ion-neutral collision rates. Unfortunately, with the end of the dual frequency operation of EISCAT in Tromsø, multi-frequency ISR observations will be no longer available. However, it might be possible to indirectly estimate such collision frequencies by fitting full-wave scattering reflection profiles to meteor observations.

Furthermore, we demonstrate that the calculated full-wave scattering reflection coefficients can be fitted to meteor observations by SAAMER-OS using the circular total signal of the five receiving antennas forming the interferometer and two additional antennas each recording separate polarization directions. In doing so, this method becomes equivalent to the triple frequency approach of the CMOR radar. The alignment between the meteor trail and the incident radio wave was determined from the multistatic receive antennas using the time-of-flight method (Mazur et al., 2020; Bruzzone et al., 2021), which allows for accurate and precise trajectory information of the meteor trail. In total we analyzed 33 meteors by manually fitting the reflection profile to the observations and obtained physically consistent solutions of the ambipolar diffusion coefficient, the initial trail radius, and the electron line density. We tested the consistency to derive ambipolar diffusion coefficients from the echo profile decay time and extracted deviations from the classical theory to the full-wave scatter solution as deviations of the T_e/T_i-ratio. While we confirmed the general applicability of the method, we also found significant differences for transition-type echoes, even though these meteors still show an exponential decay. The previous assumption of neglecting the electron–ion collisions seems to be only valid once the meteor trail started to diffuse. Instead, it appears that these Coulomb collisions (electron–electron and electron–ion) play a major role at all altitudes of the meteor layer between 70–110 km at the initial stage of the trail formation when the plasma density is still high. Later, when the plasma started to diffuse and the plasma density starts to decrease, the electron-neutral collisions become a leading order effect at altitudes below 90 km due to the increased atmospheric density.

CRediT authorship contribution statement

Gunter Stober: Gunter Stober is a member of the Oeschger Center for Climate Change Research (OCCR). Calculations were performed on UBELIX (http://www.id.unibe.ch/hpc, last access: 04 May 2023), the HPC cluster at the University of Bern. GS performed the full-wave scattering simulations and implemented the data analysis. All authors discussed the results and edited the manuscript. **Robert Weryk:** DJ and RW had conceptualized the idea of polarization measurements on SAAMER and RW computed all orbital parameters and selected the meteors. RW is supported by the Pan-STARRS survey of the Institute for Astronomy at the University of Hawaii. All authors discussed the results and edited the manuscript. **Diego Janches:** DJ and RW had conceptualized the idea of polarization measurements on SAAMER and DJ is responsible for the operation and coordination of the system. Support for DJ, ECMD as well as SAAMER-OS' operation are provided by NASA's Planetary Science Division Research Program, through ISFM work package Exospheres, Ionospheres, Magnetospheres Modeling at Goddard Space Flight Center and NASA Engineering Safety Center (NESC) assessment TI-17-01204. This work was supported in part by the NASA Meteoroid Environment Office under cooperative agreement no. 80NSSC18M0046. All authors discussed the results and edited the manuscript. **Erin C.M. Dawkins:** Support for DJ, ECMD as well as SAAMER-OS' operation are provided by NASA's Planetary Science Division Research Program, through ISFM work package Exospheres, Ionospheres, Magnetospheres Modeling at Goddard Space Flight Center and NASA Engineering Safety Center (NESC) assessment TI-17-01204. This work was supported in part by the NASA Meteoroid Environment Office under cooperative agreement no. 80NSSC18M0046. All authors discussed the results and edited the manuscript. **Florian Günzkofer:** FG prepared the EISCAT experiments and analyzed the EISCAT data. EISCAT is an international association supported by research organizations in China (CRIRP), Finland (SA), Japan (NIPR and ISEE), Norway (NFR), Sweden (VR), and the United Kingdom (UKRI). All authors discussed the results and edited the manuscript. **Jose Luis Hormaechea:** All authors discussed the results and edited the manuscript. **Dimitry Pokhotelov:** DP supported the EISCAT experiments and supervised the EISCAT data analysis by FG. All authors discussed the results and edited the manuscript.

Declaration of competing interest

The authors declare the following financial interests/personal relationships which may be considered as potential competing interests: Erin C.M. Dawkins reports financial support was provided by NASA Engineering Safety Center (NESC) assessment TI-17-01204. Diego Janches reports financial support was provided by NASA Meteoroid Environment Office under cooperative agreement no. 80NSSC18M0046. Gunter Stober reports financial support was provided by Oeschger Center for Climate Change Research. Joined patent: https://wiley.altmetric.com/details/4055199/patents

Data availability

Data will be made available on request.

References

Baggaley, W., 2002. Radar observations. In: Murad, E., Williams, I. (Eds.), Meteors in the Earth's Atmosphere. Cambridge Univ Press, Cambridge, U.K., pp. 123–147.

Bruzzone, J.S., Weryk, R.J., Janches, D., Baumann, C., Stober, G., Hormaechea, J.L., 2021. Observation of the a Carinid meteor shower 2020 unexpected outburst. Planet. Sci. J. 2 (2), 56. http://dx.doi.org/10.3847/PSJ/abe9af.

Callen, J.D., 2006. Fundamentals of Plasma Physics. Univ. of Wisconsin, Madison.

Campbell-Brown, M.D., Jones, J., 2006. Annual variation of sporadic radar meteor rates. Mon. Not. R. Astron. Soc. 367 (2), 709–716. http://dx.doi.org/10.1111/j.1365-2966.2005.09974.x, arXiv:https://academic.oup.com/mnras/article-pdf/367/2/709/3307650/367-2-709.pdf.

Cash, J., Karp, A., 1990. A variable order Runge-Kutta method for initial value problems with rapidly varying right-hand sides. ACM Trans. Math. Softw. 16, 201–222. http://dx.doi.org/10.1145/79505.79507.

Ceplecha, Z., Borovička, J., Elford, W.G., ReVelle, D.O., Hawkes, R.L., Porubčan, V., Šimek, M., 1998. Meteor phenomena and bodies. Space Sci. Rev. 84 (3), 327–471. http://dx.doi.org/10.1023/A:1005069928850.

Chapman, S., 1956. The electrical conductivity of the ionosphere: A review. Il Nuovo Cimento 4 (S4), 1385–1412. http://dx.doi.org/10.1007/BF02746310.

Chilson, P.B., Czechowsky, P., Schmidt, G., 1996. A comparison of ambipolar diffusion coefficients in meteor trains using VHF radar and UV lidar. Geophys. Res. Lett. 23 (20), 2745–2748. http://dx.doi.org/10.1029/96GL02577, arXiv:https://agupubs.onlinelibrary.wiley.com/doi/pdf/10.1029/96GL02577, URL: https://agupubs.onlinelibrary.wiley.com/doi/abs/10.1029/96GL02577.

Dawkins, E.C.M., Stober, G., Janches, D., Carrillo-Sánchez, J.D., Lieberman, R.S., Jacobi, C., Moffat-Griffin, T., Mitchell, N.J., Cobbett, N., Batista, P.P., Andrioli, V.F., Buriti, R.A., Murphy, D.J., Kero, J., Gulbrandsen, N., Tsutsumi, M., Kozlovsky, A., Kim, J.H., Lee, C., Lester, M., 2023. Solar cycle and long-term trends in the observed peak of the meteor altitude distributions by meteor radars. Geophys. Res. Lett. 50 (2), http://dx.doi.org/10.1029/2022GL101953, arXiv:https://agupubs.onlinelibrary.wiley.com/doi/pdf/10.1029/2022GL101953, URL: https://agupubs.onlinelibrary.wiley.com/doi/abs/10.1029/2022GL101953, e2022GL101953 2022GL101953.

De Oliveira-Costa, A., Tegmark, M., Gaensler, B.M., Jonas, J., Landecker, T.L., Reich, P., 2008. A model of diffuse Galactic radio emission from 10 MHz to 100 GHz. Mon. Not. R. Astron. Soc. 388 (1), 247–260. http://dx.doi.org/10.1111/j.1365-2966.2008.13376.x, arXiv:https://onlinelibrary.wiley.com/doi/pdf/10.1111/j.1365-2966.2008.13376.x, URL: https://onlinelibrary.wiley.com/doi/abs/10.1111/j.1365-2966.2008.13376.x.

de Wit, R.J., Janches, D., Fritts, D.C., Hibbins, R.E., 2016. QBO modulation of the mesopause gravity wave momentum flux over Tierra del Fuego. Geophys. Res. Lett. 43 (8), 4049–4055. http://dx.doi.org/10.1002/2016GL068599, arXiv:https://agupubs.onlinelibrary.wiley.com/doi/pdf/10.1002/2016GL068599, URL: https://agupubs.onlinelibrary.wiley.com/doi/abs/10.1002/2016GL068599.

de Wit, R.J., Janches, D., Fritts, D.C., Stockwell, R.G., Coy, L., 2017. Unexpected climatological behavior of MLT gravity wave momentum flux in the lee of the Southern Andes hot spot. Geophys. Res. Lett. 44 (2), 1182–1191. http://dx.doi.org/10.1002/2016GL072311, arXiv:https://agupubs.onlinelibrary.wiley.com/doi/pdf/10.1002/2016GL072311, URL: https://agupubs.onlinelibrary.wiley.com/doi/abs/10.1002/2016GL072311.

Dimant, Y.S., Oppenheim, M.M., 2006a. Meteor trail diffusion and fields: 1. Simulations. J. Geophys. Res. Space Phys. 111 (A12), http://dx.doi.org/10.1029/2006JA011797, arXiv:https://agupubs.onlinelibrary.wiley.com/doi/pdf/10.1029/2006JA011797, URL: https://agupubs.onlinelibrary.wiley.com/doi/abs/10.1029/2006JA011797.

Dimant, Y.S., Oppenheim, M.M., 2006b. Meteor trail diffusion and fields: 2. Analytical theory. J. Geophys. Res. Space Phys. 111 (A12), http://dx.doi.org/10.1029/2006JA011798, arXiv:https://agupubs.onlinelibrary.wiley.com/doi/pdf/10.1029/2006JA011798, URL: https://agupubs.onlinelibrary.wiley.com/doi/abs/10.1029/2006JA011798.

Dimant, Y.S., Oppenheim, M.M., 2017a. Formation of plasma around a small meteoroid: 1. Kinetic theory. J. Geophys. Res. Space Phys. 122 (4), 4669–4696. http://dx.doi.org/10.1002/2017JA023960, arXiv:1608.08524, URL: http://doi.wiley.com/10.1002/2017JA023960.

Dimant, Y.S., Oppenheim, M.M., 2017b. Formation of plasma around a small meteoroid: 2. Implications for radar head echo. J. Geophys. Res. Space Phys. 122 (4), 4697–4711. http://dx.doi.org/10.1002/2017JA023963, arXiv:1608.08524, URL: http://doi.wiley.com/10.1002/2017JA023963.

Elford, W.G., 2004. Radar observations of meteor trails, and their interpretation using fresnel holography: A new tool in meteor science. Atmos. Chem. Phys. 4 (4), 911–921. http://dx.doi.org/10.5194/acp-4-911-2004, URL: https://acp.copernicus.org/articles/4/911/2004/.

Fritts, D.C., Janches, D., Iimura, H., Hocking, W.K., Mitchell, N.J., Stockwell, R.G., Fuller, B., Vandepeer, B., Hormaechea, J., Brunini, C., Levato, H., 2010. Southern Argentina agile meteor radar: System design and initial measurements of large-scale winds and tides. J. Geophys. Res.: Atmos. 115 (D18), http://dx.doi.org/10.1029/2010JD013850, arXiv:https://agupubs.onlinelibrary.wiley.com/doi/pdf/10.1029/2010JD013850, URL: https://agupubs.onlinelibrary.wiley.com/doi/abs/10.1029/2010JD013850.

Grassmann, V., 1993. An incoherent scatter experiment for the measurement of particle collisions. J. Atmos. Terr. Phys. 55 (4–5), 573–576. http://dx.doi.org/10.1016/0021-9169(93)90006-K.

Greenhow, J.S., Hall, J., 1960. The importance of initial trail radius on the apparent height and number distributions of meteor echoes. Mon. Not. R. Astron. Soc. 121, 183, URL: http://adsabs.harvard.edu/full/1960MNRAS.121..183G.

Hedin, A.E., 1991. Extension of the MSIS thermosphere model into the middle and lower atmosphere. J. Geophys. Res. Space Phys. 96 (A2), 1159–1172. http://dx.doi.org/10.1029/90JA02125, arXiv:https://agupubs.onlinelibrary.wiley.com/doi/pdf/10.1029/90JA02125, URL: https://agupubs.onlinelibrary.wiley.com/doi/abs/10.1029/90JA02125.

Herlofson, N., 1951. Ark. Fys. 3, 247.

Hocking, W.K., 1999. Temperatures using radar-meteor decay times. Geophys. Res. Lett. 26 (21), 3297–3300. http://dx.doi.org/10.1029/1999GL003618, arXiv:https://agupubs.onlinelibrary.wiley.com/doi/pdf/10.1029/1999GL003618, URL: https://agupubs.onlinelibrary.wiley.com/doi/abs/10.1029/1999GL003618.

Hocking, W.K., 2000. Real-time meteor entrance speed determinations made with interferometric meteor radars. Radio Sci. 35 (5), 1205–1220. http://dx.doi.org/10.1029/1999RS002283.

Hocking, W., Fuller, B., Vandepeer, B., 2001. Real-time determination of meteor-related parameters utilizing modern digital technology. J. Atmos. Sol.-Terr. Phys. 63, 155–169. http://dx.doi.org/10.1016/S1364-6826(00)00138-3, URL: http://www.sciencedirect.com/science/article/pii/S1364682600001383, Radar applications for atmosphere and ionosphere research - PIERS 1999.

Hocking, W., Singer, W., Bremer, J., Mitchell, N., Batista, P., Clemesha, B., Donner, M., 2004. Meteor radar temperatures at multiple sites derived with SKiYMET radars and compared to OH, rocket and lidar measurements. J. Atmos. Sol.-Terr. Phys. 66 (6), 585–593. http://dx.doi.org/10.1016/j.jastp.2004.01.011, URL: https://www.sciencedirect.com/science/article/pii/S1364682604000227, Dynamics and Chemistry of the MLT Region - PSMOS 2002 International Symposium.

Hocking, W.K., Thayaparan, T., Jones, J., 1997. Meteor decay times and their use in determining a diagnostic mesospheric temperature-pressure parameter: Methodology and one year of data. Geophys. Res. Lett. 24 (23), 2977–2980. http://dx.doi.org/10.1029/97GL03048.

Holdsworth, D.A., Elford, W.G., Vincent, R.A., Reid, I.M., Murphy, D.J., Singer, W., 2007. All-sky interferometric meteor radar meteoroid speed estimation using the fresnel transform. Ann. Geophys. 25 (2), 385–398. http://dx.doi.org/10.5194/angeo-25-385-2007, URL: https://angeo.copernicus.org/articles/25/385/2007/.

Holdsworth, D.A., Morris, R.J., Murphy, D.J., Reid, I.M., Burns, G.B., French, W.J.R., 2006. Antarctic mesospheric temperature estimation using the davis mesosphere-stratosphere-troposphere radar. J. Geophys. Res.: Atmos. 111 (D5), http://dx.doi.org/10.1029/2005JD006589, arXiv:https://agupubs.onlinelibrary.wiley.com/doi/pdf/10.1029/2005JD006589, URL: https://agupubs.onlinelibrary.wiley.com/doi/abs/10.1029/2005JD006589.

Holdsworth, D.A., Reid, I.M., 2002. The buckland park meteor radar - description and initial results. In: Workshop on Applications of Radio Science, Int. Union of Radio Sci., Leura, Australia.

Holdsworth, D.A., Reid, I.M., Cervera, M.A., 2004. Buckland park all-sky interferometric meteor radar. Radio Sci. 39 (5), http://dx.doi.org/10.1029/2003RS003014, arXiv:https://agupubs.onlinelibrary.wiley.com/doi/pdf/10.1029/2003RS003014, URL: https://agupubs.onlinelibrary.wiley.com/doi/abs/10.1029/2003RS003014.

Jacobs, E., Ralston, E.W., 1981. Ambiguity resolution in interferometry. IEEE Trans. Aerosp. Electron. Syst. AES-17 (6), 766–780.

Janches, D., Bruzzone, J.S., Weryk, R.J., Hormaechea, J.L., Wiegert, P., Brunini, C., 2020. Observations of an unexpected meteor shower outburst at high ecliptic southern latitude and its potential origin. Astrophys. J. Lett. 895 (1), L25. http://dx.doi.org/10.3847/2041-8213/ab9181.

Janches, D., Close, S., Fentzke, J.T., 2008. A comparison of detection sensitivity between ALTAIR and Arecibo meteor observations: Can high power and large aperture radars detect low velocity meteor head-echoes. Icarus 193 (1), 105–111. http://dx.doi.org/10.1016/j.icarus.2007.08.022, URL: https://www.sciencedirect.com/science/article/pii/S0019103507003648.

Janches, D., Close, S., Hormaechea, J.L., Swarnalingam, N., Murphy, A., O'Connor, D., Vandepeer, B., Fuller, B., Fritts, D.C., Brunini, C., 2015. THE SOUTHERN Argentina agile meteor radar orbital system (Saamer-OS): An initial sporadic meteoroid orbital survey in the southern sky. Astrophys. J. 809 (1), 36. http://dx.doi.org/10.1088/0004-637x/809/1/36.

Janches, D., Hocking, W., Pifko, S., Hormaechea, J.L., Fritts, D.C., Brunini, C., Michell, R., Samara, M., 2014. Interferometric meteor head echo observations using the southern Argentina agile meteor radar. J. Geophys. Res. Space Phys. 119, http://dx.doi.org/10.1002/2013JA019241.

Janches, D., Nolan, M.C., Meisel, D.D., Mathews, J.D., Zhou, Q.H., Moser, D.E., 2003. On the geocentric micrometeor velocity distribution. J. Geophys. Res. Space Phys. 108 (A6), http://dx.doi.org/10.1029/2002JA009789, arXiv:https://agupubs.onlinelibrary.wiley.com/doi/pdf/10.1029/2002JA009789, URL: https://agupubs.onlinelibrary.wiley.com/doi/abs/10.1029/2002JA009789.

Jones, J., 1975. On the decay of underdense radio meteor echoes. Mon. Not. R. Astron. Soc. 173 (3), 637–647. http://dx.doi.org/10.1093/mnras/173.3.637, arXiv:https://academic.oup.com/mnras/article-pdf/173/3/637/2929013/mnras173-0637.pdf.

Jones, J., Brown, P., Ellis, K., Webster, A., Campbell-Brown, M., Krzemenski, Z., Weryk, R., 2005. The Canadian meteor orbit radar: System overview and preliminary results. Planet. Space Sci. 53 (4), 413–421. http://dx.doi.org/10.1016/j.pss.2004.11.002, URL: https://www.sciencedirect.com/science/article/pii/S0032063304002302.

Jones, J., Jones, W., 1990. Oblique-scatter of radio waves from meteor trains: long wavelength approximation. Planet. Space Sci. 38 (7), 925–932. http://dx.doi.org/10.1016/0032-0633(90)90059-Y, URL: https://www.sciencedirect.com/science/article/pii/003206339090059Y.

Jones, J., Webster, A.R., Hocking, W.K., 1998. An improved interferometer design for use with meteor radars. Radio Sci. 33 (1), 55–65. http://dx.doi.org/10.1029/97RS03050.

Kaiser, T., 1953. Radio echo studies of meteor ionization. Adv. Phys. 2 (8), 495–544. http://dx.doi.org/10.1080/00018735300101282.

Kaiser, T., Closs, R., 1952a. I. Theory of radio reflections from meteor trails: I. Lond. Edinb. Dub. Philos. Mag. J. Sci. 43 (336), 1–32. http://dx.doi.org/10.1080/14786440108520963.

Kaiser, T., Closs, R.L., 1952b. Theory of radio reflections from meteor trails: I. Phil. Mag. 43 (No 336, January), 1–32.

Kaiser, T., Pickering, W., Watkins, C., 1969. Ambipolar diffusion and motion of ion clouds in the earth's magnetic field. Planet. Space Sci. 17 (3), 519–552. http://dx.doi.org/10.1016/0032-0633(69)90083-X, URL: https://www.sciencedirect.com/science/article/pii/003206336990083X.

Kero, J., Fujiwara, Y., Abo, M., Szasz, C., Nakamura, T., 2012. MU radar head echo observations of the 2011 October Draconids. Mon. Not. R. Astron. Soc. 424 (3), 1799–1806. http://dx.doi.org/10.1111/j.1365-2966.2012.21255.x, arXiv:https://academic.oup.com/mnras/article-pdf/424/3/1799/2983241/424-3-1799.pdf.

Kero, J., Szasz, C., Nakamura, T., 2013. MU head echo observations of the 2010 Geminids: Radiant, orbit, and meteor flux observing biases. Ann. Geophys. 31 (3), 439–449. http://dx.doi.org/10.5194/angeo-31-439-2013, URL: http://www.ann-geophys.net/31/439/2013/.

Kumar, K.K., Subrahmanyam, K.V., 2012. A discussion on the assumption of ambipolar diffusion of meteor trails in the Earth's upper atmosphere. Mon. Not. R. Astron. Soc.: Letters 425 (1), L1–L5. http://dx.doi.org/10.1111/j.1745-3933.2012.01279.x, arXiv:https://academic.oup.com/mnrasl/article-pdf/425/1/L1/6278844/425-1-L1.pdf.

Laskar, F.I., Stober, G., Fiedler, J., Oppenheim, M.M., Chau, J.L., Pallamraju, D., Pedatella, N.M., Tsutsumi, M., Renkwitz, T., 2019. Mesospheric anomalous diffusion during noctilucent cloud scenarios. Atmos. Chem. Phys. 19 (7), 5259–5267. http://dx.doi.org/10.5194/acp-19-5259-2019, URL: https://acp.copernicus.org/articles/19/5259/2019/.

Lee, C., Kim, J.-H., Jee, G., Lee, W., Song, I.-S.H., 2016. New method of estimating temperatures near the mesopause region using meteor radar observations. Geophys. Res. Lett. 43 (20), 10,580–10,585. http://dx.doi.org/10.1002/2016GL071082, arXiv:https://agupubs.onlinelibrary.wiley.com/doi/pdf/10.1002/2016GL071082, URL: https://agupubs.onlinelibrary.wiley.com/doi/abs/10.1002/2016GL071082.

Liu, G., Janches, D., Lieberman, R.S., Moffat-Griffin, T., Fritts, D.C., Mitchell, N.J., 2020. Coordinated observations of 8- and 6-hr tides in the mesosphere and lower thermosphere by three meteor radars near 60°S latitude. Geophys. Res. Lett. 47 (1), http://dx.doi.org/10.1029/2019GL086629, arXiv:https://agupubs.onlinelibrary.wiley.com/doi/pdf/10.1029/2019GL086629, URL: https://agupubs.onlinelibrary.wiley.com/doi/abs/10.1029/2019GL086629, e2019GL086629 2019GL086629.

Liu, G., Janches, D., Ma, J., Lieberman, R.S., Stober, G., Moffat-Griffin, T., Mitchell, N.J., Kim, J.-H., Lee, C., Murphy, D.J., 2022. Mesosphere and lower thermosphere winds and tidal variations during the 2019 antarctic sudden stratospheric warming. J. Geophys. Res. Space Phys. 127 (3), http://dx.doi.org/10.1029/2021JA030177, arXiv:https://agupubs.onlinelibrary.wiley.com/doi/pdf/10.1029/2021JA030177, URL: https://agupubs.onlinelibrary.wiley.com/doi/abs/10.1029/2021JA030177, e2021JA030177 2021JA030177.

Lovell, A., Clegg, J., 1948. Characteristics of radio echoes from meteor trails : I . The intensity of the radio reflections and electron density in the trails. Proc. Phys. Soc. 60, 491.

Marshall, R.A., Brown, P., Close, S., 2017. Plasma distributions in meteor head echoes and implications for radar cross section interpretation. Planet. Space Sci. 143, 203–208. http://dx.doi.org/10.1016/j.pss.2016.12.011, URL: http://www.sciencedirect.com/science/article/pii/S0032063316303130, SI:Meteoroids 2016.

Marshall, R.A., Close, S., 2015. An FDTD model of scattering from meteor head plasma. J. Geophys. Res. Space Phys. 120 (7), 5931–5942. http://dx.doi.org/10.1002/2015JA021238, arXiv:https://agupubs.onlinelibrary.wiley.com/doi/pdf/10.1002/2015JA021238, URL: https://agupubs.onlinelibrary.wiley.com/doi/abs/10.1002/2015JA021238.

Mazur, M., Pokorný, P., Brown, P., Weryk, R.J., Vida, D., Schult, C., Stober, G., Agrawal, A., 2020. Precision measurements of radar transverse scattering speeds from meteor phase characteristics. Radio Sci. 55 (10), 1–32. http://dx.doi.org/10.1029/2019RS006987, URL: https://onlinelibrary.wiley.com/doi/10.1029/2019RS006987.

McKinley, D.W.R., 1961. Meteor Science and Engineering.

Nicolls, M.J., Bahcivan, H., Häggström, I., Rietveld, M., 2014. Direct measurement of lower thermospheric neutral density using multifrequency incoherent scattering. Geophys. Res. Lett. 41 (23), 8147–8154. http://dx.doi.org/10.1002/2014GL062204, arXiv:https://agupubs.onlinelibrary.wiley.com/doi/pdf/10.1002/2014GL062204, URL: https://agupubs.onlinelibrary.wiley.com/doi/abs/10.1002/2014GL062204.

Nygrén, T., 1996. Studies of the E-region ion-neutral collision frequency using the EISCAT incoherent scatter radar. Adv. Space Res. 18 (3), 79–82. http://dx.doi.org/10.1016/0273-1177(95)00843-4, URL: https://www.sciencedirect.com/science/article/pii/0273117795008434, Thermosphere-Ionosphere-Middle Atmosphere Coupling and Dynamics.

Oyama, S., Kurihara, J., Watkins, B.J., Tsuda, T.T., Takahashi, T., 2012. Temporal variations of the ion-neutral collision frequency from EISCAT observations in the polar lower ionosphere during periods of geomagnetic disturbances. J. Geophys. Res. Space Phys. 117 (A5), http://dx.doi.org/10.1029/2011JA017159, arXiv:https://agupubs.onlinelibrary.wiley.com/doi/pdf/10.1029/2011JA017159, URL: https://agupubs.onlinelibrary.wiley.com/doi/abs/10.1029/2011JA017159.

Panka, P.A., Weryk, R.J., Bruzzone, J.S., Janches, D., Schult, C., Stober, G., Hormaechea, J.L., 2021. An improved method to measure head echoes using a meteor radar. Planet. Sci. J. 2 (5), 197. http://dx.doi.org/10.3847/psj/ac22b2.

Poulter, E., Baggaley, W., 1977. Radiowave scattering from meteoric ionization. J. Atmos. Terr. Phys. 39 (7), 757–768. http://dx.doi.org/10.1016/0021-9169(77)90137-4, URL: http://www.sciencedirect.com/science/article/pii/0021916977901374.

Poulter, E., Baggaley, W., 1978. The applications of radio-wave scattering theory to radio-meteor observations. Planet. Space Sci. 26 (10), 969–977. http://dx.doi.org/10.1016/0032-0633(78)90079-X, URL: http://www.sciencedirect.com/science/article/pii/003206337890079X.

Sarkar, E., Kozlovsky, A., Ulich, T., Virtanen, I., Lester, M., Kaifler, B., 2021. Improved method of estimating temperatures at meteor peak heights. Atmos. Meas. Tech. 14 (6), 4157–4169. http://dx.doi.org/10.5194/amt-14-4157-2021, URL: https://amt.copernicus.org/articles/14/4157/2021/.

Schult, C., Stober, G., Janches, D., Chau, J.L., 2017. Results of the first continuous meteor head echo survey at polar latitudes. Icarus 297, 1–13. http://dx.doi.org/10.1016/j.icarus.2017.06.019, URL: http://www.sciencedirect.com/science/article/pii/S0019103516303761.

Schunk, R., Nagy, A., 2009. Ionospheres: Physics, Plasma Physics, and Chemistry, second ed. In: Cambridge Atmospheric and Space Science Series, Cambridge University Press, http://dx.doi.org/10.1017/CBO9780511635342.

Stober, G., 2009. Astrophysical Studies on Meteors using a SKiYMET All-Sky Meteor Radar. In: Wissenschaftliche Mitteilungen aus dem Institut für Meteorologie der Universität Leipzig und dem Institut für Troposphärenforschung e. V. Leipzig, Institut für Meteorologie der Universität Leipzig.

Stober, G., Brown, P., Campbell-Brown, M., Weryk, R.J., 2021a. Triple-frequency meteor radar full wave scattering - Measurements and comparison to theory. Astron. Astrophys. 654, A108. http://dx.doi.org/10.1051/0004-6361/202141470.

Stober, G., Jacobi, C., Fröhlich, K., Oberheide, J., 2008. Meteor radar temperatures over collm (51.3°n, 13°e). Adv. Space Res. 42 (7), 1253–1258. http://dx.doi.org/10.1016/j.asr.2007.10.018.

Stober, G., Jacobi, C., Matthias, V., Hoffmann, P., Gerding, M., 2012. Neutral air density variations during strong planetary wave activity in the mesopause region derived from meteor radar observations. J. Atmos. Sol.-Terr. Phys. 74, 55–63. http://dx.doi.org/10.1016/j.jastp.2011.10.007, URL: https://www.sciencedirect.com/science/article/pii/S136468261100280X.

Stober, G., Kozlovsky, A., Liu, A., Qiao, Z., Tsutsumi, M., Hall, C., Nozawa, S., Lester, M., Belova, E., Kero, J., Espy, P.J., Hibbins, R.E., Mitchell, N., 2021b. Atmospheric tomography using the nordic meteor radar cluster and Chilean observation network de meteor radars: network details and 3D-Var retrieval. Atmos. Meas. Tech. 14 (10), 6509–6532. http://dx.doi.org/10.5194/amt-14-6509-2021, URL: https://amt.copernicus.org/articles/14/6509/2021/.

Stober, G., Kuchar, A., Pokhotelov, D., Liu, H., Liu, H.-L., Schmidt, H., Jacobi, C., Baumgarten, K., Brown, P., Janches, D., Murphy, D., Kozlovsky, A., Lester, M., Belova, E., Kero, J., Mitchell, N., 2021c. Interhemispheric differences of mesosphere–lower thermosphere winds and tides investigated from three whole-atmosphere models and meteor radar observations. Atmos. Chem. Phys. 21 (18), 13855–13902. http://dx.doi.org/10.5194/acp-21-13855-2021, URL: https://acp.copernicus.org/articles/21/13855/2021/.

Stober, G., Liu, A., Kozlovsky, A., Qiao, Z., Kuchar, A., Jacobi, C., Meek, C., Janches, D., Liu, G., Tsutsumi, M., Gulbrandsen, N., Nozawa, S., Lester, M., Belova, E., Kero, J., Mitchell, N., 2022. Meteor radar vertical wind observation biases and mathematical debiasing strategies including the 3DVAR+DIV algorithm. Atmos. Meas. Tech. 15 (19), 5769–5792. http://dx.doi.org/10.5194/amt-15-5769-2022, URL: https://amt.copernicus.org/articles/15/5769/2022/.

Stober, G., Matthias, V., Jacobi, C., Wilhelm, S., Höffner, J., Chau, J.L., 2017. Exceptionally strong summer-like zonal wind reversal in the upper mesosphere during winter 2015/16. Ann. Geophys. 35 (3), 711–720. http://dx.doi.org/10.5194/angeo-35-711-2017, URL: https://www.ann-geophys.net/35/711/2017/.

Stober, G., Schult, C., Baumann, C., Latteck, R., Rapp, M., 2013. The geminid meteor shower during the ECOMA sounding rocket campaign: Specular and head echo radar observations. Ann. Geophys. 31 (3), 473–487. http://dx.doi.org/10.5194/angeo-31-473-2013, URL: https://angeo.copernicus.org/articles/31/473/2013/.

Stober, G., Singer, W., Jacobi, C., 2011. Cosmic radio noise observations using a mid-latitude meteor radar. J. Atmos. Sol.-Terr. Phys. 73 (9), 1069–1076. http://dx.doi.org/10.1016/j.jastp.2010.07.018, URL: https://www.sciencedirect.com/science/article/pii/S1364682610002142, Scientific Results from Networked and Multi-instrument studies based on MST Radar.

Sugar, G., Oppenheim, M.M., Dimant, Y.S., Close, S., 2018. Formation of plasma around a small meteoroid: Simulation and theory. J. Geophys. Res. Space Phys. 123 (5), 4080–4093. http://dx.doi.org/10.1002/2018JA025265, URL: http://doi.wiley.com/10.1002/2018JA025265.

Sugar, G., Oppenheim, M.M., Dimant, Y., Close, S., 2019. Formation of plasma around a small meteoroid: Electrostatic simulations. J. Geophys. Res. Space Phys. (May), 3810–3826. http://dx.doi.org/10.1029/2018ja026434.

Swarnalingam, N., Hocking, W.K., Argall, P.S., 2009. Radar efficiency and the calculation of decade-long PMSE backscatter cross-section for the Resolute Bay VHF radar. Ann. Geophys. 27 (4), 1643–1656. http://dx.doi.org/10.5194/angeo-27-1643-2009, URL: https://angeo.copernicus.org/articles/27/1643/2009/.

Vida, D., Brown, P.G., Campbell-Brown, M., Weryk, R.J., Stober, G., McCormack, J.P., 2021. High precision meteor observations with the canadian automated meteor observatory: data reduction pipeline and application to meteoroid mechanical strength measurements. Icarus 354, 114097. http://dx.doi.org/10.1016/j.icarus.2020.114097.

Webster, A.R., Brown, P.G., Jones, J., Ellis, K.J., Campbell-Brown, M., 2004. Canadian Meteor Orbit Radar (CMOR). Atmos. Chem. Phys. 4 (3), 679–684. http://dx.doi.org/10.5194/acp-4-679-2004, URL: https://www.atmos-chem-phys.net/4/679/2004/.

Ye, Q.-Z., Han, S.X., 2017. Ozone measurements with meteors: A revisit. Mon. Not. R. Astron. Soc. 472 (1), 2–7. http://dx.doi.org/10.1093/mnras/stx1851, arXiv:https://academic.oup.com/mnras/article-pdf/472/1/2/19678979/stx1851.pdf.